T. Hiraga · I.M. Anderson · M.E. Zimmerman · S. Mei
D.L. Kohlstedt

Structure and chemistry of grain boundaries in deformed, olivine + basalt and partially molten lherzolite aggregates: evidence of melt-free grain boundaries

Abstract Olivine grain boundaries in deformed aggregates of olivine + basalt and partially molten lherzolite were analyzed with various electron microscopy techniques to test for the presence of thin (0.5–10 nm) intergranular melt films. High-resolution transmission electron microscopy (HREM) observations reveal that most of the boundaries do not contain a thin amorphous phase, although a small fraction of grains are separated by relatively thick ($\sim$1 μm) layers of melt. However, due to the anisotropy of the olivine-melt interfacial energy, melt often tapers from a triple junction into an adjoining grain boundary over a length of 1 to 2 μm, giving an effective dihedral angle of only $\sim$2°. The chemistry of olivine-olivine grain boundaries was analyzed using energy dispersive X-ray (EDX) profiling by scanning transmission electron microscopy (STEM) with a probe size of < 1.5 nm. Ca, Al and Ti segregate to grain boundaries forming enriched regions of < 7 nm width. Although these elements are concentrated in the glass phases, the presence of glass films with the same chemical composition as the bulk glass phases cannot explain concentrations of other elements such as Si and Al at the boundaries. Combined with the HREM results, the STEM/EDX profiling demonstrates the existence of chemical segregation between solid grains but the absence of thin, grain boundary melt films. Additionally, if melt films exist along all of the grain boundaries, as reported for similar samples by other groups, the rock should be substantially weakened. Creep experiments on the partially molten rocks analyzed in this study reveal little weakening at small melt contents, consistent with our observations of melt-free grain boundaries.

T. Hiraga (✉) · M.E. Zimmerman · S. Mei · D.L. Kohlstedt
Department of Geology and Geophysics,
University of Minnesota, Minneapolis, MN 55455, USA
E-mail: hirag001@umn.edu

I.M. Anderson
Metals and Ceramics Division,
Oak Ridge National Laboratory,
Oak Ridge TN 37831, USA

Editorial responsibility: T.L. Grove

Introduction

Studies of grain boundaries in partially molten ultramafic rocks have led to two conflicting conclusions: nanometer-thick melt film wet grain boundaries (Drury and Fitz Gerald 1996; De Kloe et al. 2000) versus essentially all grain boundaries being melt-free (Vaughan et al. 1982; Kohlstedt 1990). Following previous studies, a melt film is defined as an intergranular melt phase with a characteristic thickness in the range 0.5 to 10 nm. The presence of melt films is well documented in some sintered materials such as silicon nitride ceramics. The stability of the film and its thickness are controlled by the balance between attractive van der Waals forces and repulsive steric forces (Clarke 1987), and its atomic structure is different from that of a bulk melt due to these forces. Since films are fast diffusion paths and enhance grain boundary sliding, the presence of films can significantly weaken a material (e.g., Hwang and Chen 1990). Thus, it is important to determine the presence or absence of stable melt films in partially molten rocks having a low melt fraction, to permit understanding of the dynamics of partially molten regions such as those beneath mid-ocean ridges and island arcs.

Several possible reasons were suggested by De Kloe et al. (2000) for the conclusion reached by other investigators that films are absent. (1) Systems differ from one another based on melt composition. Papers which support grain boundary wetting examined pyroxene-bearing rocks, whereas the others studied olivine-basalt aggregates without pyroxenes. (2) Energy dispersive X-ray analysis was not precise enough to detect X-ray peaks from a thin melt film because of irradiation damage or misalignment of the beam with respect to the boundaries. (3) The time-at-temperature for samples without

melt films was not long enough for the aggregate to reach a stable microstructure.

In this paper, we use high-resolution analyses of grain boundary structure and chemistry to demonstrate that melt films are not present and to suggest reasons for the contradictory conclusions. We used three techniques: high-resolution transmission electron microscopy (HREM), energy dispersive X-ray (EDX) profiling in the scanning transmission electron microscopy (STEM) mode, and low-voltage (LV) energy dispersive X-ray (EDX) spectrum imaging in a scanning electron microscope (SEM). De Kloe et al. (2000) used several TEM techniques to test for the presence of films, since they determined that individually each of the methods which they used was inconclusive. However, one of the methods they used, HREM, is capable of revealing the detailed structure of grain boundaries containing a glass film (Cinibulk et al. 1993). As shown below, HREM images require very careful interpretation. Chemical analysis of the same boundary provides further evidence for the presence or absence of an intergranular melt film. Previous studies have shown that boundaries are enriched in Ca and Al but depleted in Mg relative to the grains, which led to the conclusion that a glass film was present (Drury and Fitz Gerald 1996; De Kloe et al. 2000). However, these chemical signatures can also be caused by chemical segregation to the solid-solid boundaries without forming a specific grain boundary phase (e.g., Kingery 1974). To determine the presence or absence of a glass film, the behavior of other elements at grain boundaries must be known at the nanometer scale.

Samples

We chose two types of samples to study the possible existence of thin melt films: aggregates of olivine with 2–12 vol% basalt, and partially molten lherzolite which contains 9 vol% melt. Basalt was mechanically mixed with olivine powders for the former, and melt was produced in situ during hot-pressing and deformation of the lherzolite. The former was fabricated under water-saturated conditions, and the latter was synthesized under dry conditions. To investigate the effect of the melt fraction, olivine + basalt samples with different amounts of melt were analyzed. The experimental details of the olivine + basalt samples have been reported by Mei et al. (2002), and those of the partially molten lherzolite should appear in the near future (Zimmerman and Kohlstedt, unpublished data). Here, we describe the samples briefly.

Olivine + basalt aggregates

The samples were mechanically tested to determine its deformation properties, particularly the effects of water and melt on rheology (Mei et al. 2002). Samples for deformation experiments were fabricated from powdered San Carlos olivine and powdered mid-ocean ridge basalt (MORB; Daines and Kohlstedt 1993). Olivine powder of particle size < 10 μm was mixed mechanically with 1, 4 or 7 wt% MORB of particle size < 8 μm. The powders were cold-pressed into a Ni capsule under a uniaxial pressure of 200 MPa, and then isostatically hot-pressed inside the Ni capsule at 1,523 K and 300 MPa for 3 h in a gas-medium apparatus. The oxygen fugacity during hot-pressing was buffered near Ni–NiO by oxidation of the Ni capsule. To produce wet conditions, hot-pressed samples were wrapped in 0.12 mm thick nickel foil and inserted into a talc sleeve. This sample assembly was welded into a nickel capsule to minimize loss of water during the subsequent creep experiment. Samples were deformed at constant loads in a gas-medium apparatus (Paterson 1990) at a confining pressure of 300 MPa and temperatures between 1,373 and 1,473 K for ~5 h. Oxygen fugacity was buffered near Ni–NiO by oxidation of the Ni capsule and the Ni foil. Dehydration of the talc near 1,070 K provided a source of water. Creep data were obtained by varying the stress in a stepwise fashion at constant temperature and pressure or by varying temperature at constant stress and pressure. For most samples, steady-state deformation was achieved by $< 1\%$ strain. At the end of each experiment, the sample was cooled under load at a rate of ~2 K/s to 900 K. The load was then removed, and the samples were brought to ambient conditions at a cooling rate of ~1 K/s and a depressurization rate of ~1–2 MPa/s. Melting during these hydrous experiments resulted in melt percentages of 2, 8 and 12 vol%. In the diffusion creep regime, at a given differential stress, samples with melt fractions of 2 and 12 vol% deformed 2 and 30 times faster, respectively, than a melt-free sample. In the dislocation creep regime, a sample with a melt fraction of 12 vol% deformed a factor of ~25 faster than a sample with a melt fraction of 2 vol%.

Partially molten lherzolite aggregate

This sample was mechanically tested to quantify its deformation properties, specifically the influence of melt on the rheology of lherzolite (Zimmerman and Kohlstedt, unpublished data). High-density samples were fabricated by hot-pressing ground powders of spinel lherzolite, derived from a mantle xenolith from Damaping in the Hubei Province of Eastern China. The bulk mineral composition of this spinel lherzolite is 61.8 vol% olivine, 26.0 vol% orthopyroxene (OPX), 10.0 vol% clinopyroxene (CPX), and 2.2 vol% spinel. The powders with a grain size of 25–45 μm were dried in a controlled-atmosphere furnace using a mixture of $CO–CO_2$ gases to control the oxygen fugacity. The sample was subsequently hot-pressed at 1,473 K (solidus temperature = 1,433 K) and 300 MPa for 3 h in an internally heated, argon gas-medium pressure vessel. The oxygen fugacity during hot-pressing and deformation was buffered near Ni–NiO by oxidation of the Ni can. Initial

melting occurs at boundaries where all four solid phases are present. Thus, the presence of melt at boundaries with olivine as the only solid phase even at low melt fractions indicates that the melt phase is able to redistribute during hot-pressing. Triaxial compressional deformation experiments were conducted in the same apparatus. The deformation sample assembly and basic procedures are the same as those reported by Hirth and Kohlstedt (1995). Temperatures during deformation ranged from 1,473 to 1,573 K, with a confining pressure of 300 MPa and a differential stress of 36 MPa. Total deformation time was ~5 h with a 1.5 h pre-annealing time. The total strain achieved was ~15%. During this experiment, ~9 vol% melt was formed.

Electron microscopy techniques

HREM

Three well-known TEM methods have been used to study thin amorphous (i.e., quenched melt or glass) films at grain boundaries: high-resolution lattice fringe imaging, defocus Fresnel fringe imaging, and diffuse dark-field (DDF) imaging (e.g., Clarke 1979). As previous papers have pointed out, the presence of a thin film must first be confirmed by lattice imaging (Simpson et al. 1986; Cinibulk et al. 1993). Then, additional methods provide important structural information about the film, such as the distribution of the film. The reasons are as follows.

1. HREM reveals discontinuities of the lattice fringes along a boundary. The thickness of the discontinuity corresponds to the real film thickness. DDF imaging and Fresnel fringe imaging yield values 50 to 100% and 20 to 35% thicker, respectively, than the real thickness of the film (Cinibulk et al. 1993).
2. Since ion thinning preferentially removes material at boundaries, grooves develop along the grain boundaries. Amorphous material can then fill the grooves during ion milling and/or subsequent carbon coating. The result is an artificial film which cannot be distinguished from a thin glass film by the DDF technique, which uses diffusely scattered electrons from amorphous phases in the sample.
3. A grooved surface, even in the absence of a glass film, can produce Fresnel fringes with contrast stronger than that produced by a glass film at a grain boundary (Rasmussen et al. 1989).

Therefore, HREM study of grain boundaries is the only robust technique for analyzing the boundary structure. However, this technique requires that the incident beam be parallel to the grain boundary plane, the so-called edge-on condition, to examine the possible existence of thin grain boundary phases (e.g., Clarke 1979). At the same time, diffraction conditions must be established to observe lattice fringes in both of the neighboring grains.

To investigate grain boundary structure with maximum resolution, the Scherzer defocus condition is commonly used. However, since lattice fringes can extend into the boundary at the Scherzer defocus condition, we employed the through-focus method to ensure that the boundary structure does not change in going from Scherzer defocus to Gaussian focus (e.g., Cinibulk et al. 1993). Actually, this problem is not very serious for the following reason. The magnitude of the Bragg beam displacement r is given by $r = C_s(\lambda/d)^3 + \Delta f(\lambda/d)$ where C_s is a spherical aberration coefficient of the objective lens, λ the electron wave length, d the lattice fringe spacing, and Δf the defocus distance. Given the maximum values used in this study of $\Delta f = 40$ nm and $d = 0.51$ nm with constant values of $C_s = 2.0$ mm and $\lambda = 0.00197$ nm, the calculated fringe shift is $r = 0.15$ nm. This value is less than the resolution of the microscope and is much less than the film width reported for many materials.

Thin specimens for the HREM observations were prepared by ion-milling. To minimize selective thinning of the glass phase during milling, we used a Gatan Dual ion-thinner at an angle of 9° for the initial broad-region milling of the sample, and Gatan Pips thinner at 4° for the final thinning. Mineral phases comprising the samples were identified with a Philips CM30 TEM operating at 300 kV and equipped with an EDAX EDX detector and analyzer.

STEM/EDX profiling

Characteristic X-ray profiles were acquired from the same specimens used for HREM analysis with a Philips CM200 TEM/STEM equipped with a Schottky field emission gun (FEG), an Oxford EDX detector with a super atmospheric thin window and XP3 pulse processor, and an EMiSPEC (ES) Vision integrated acquisition system. In STEM mode, the incident electron probe is 1.3–1.4 nm in diameter (FWHM) with ~1 nA probe current. The probe size was directly measured from a high-magnification image using a CCD camera installed on the CM200 prior to the acquisition of the X-ray spectrum profiles from the samples. Grain boundaries were slightly misoriented from the edge-on condition to mitigate electron channeling effects in grains having low-index boundary planes.

Beam damage is a critical issue for these materials, and it was determined that the standard integrated spectrum profiling and imaging methods available with ES Vision were insufficient to yield damage-free profiles. The positioning of a stationary beam on the specimen, even for the ~200 ms necessary to collect adequate signal in the spectrum imaging mode, induced significant damage. A modified data acquisition method was therefore devised to minimize the effects of beam damage. ES Vision was used to collect a sequence of spectra, while the incident electron beam was controlled independently by the microscope so that the electron beam performed several rasters parallel to the boundary on the

specimen during the collection of a single pixel in the EDX profile. The dwell time per pixel ($\sim$200 ms) was adjusted to allow 100 spectra to be acquired over the duration of a single frame of the STEM image ($\sim$20 s). The STEM magnification was such that the pixel spacing was slightly larger than the beam diameter, $\sim$1.4 nm. By operating ES Vision in spectrum imaging mode, a time sequence of spectrum profiles was acquired from a given area on the boundary, as shown schematically in Fig. 1. The size of area was $\sim$125$\times$100 nm. Hence, grain boundaries which were flat at least over a distance of $\sim$125 nm had to be chosen for analysis to obtain a high-resolution profile near the boundaries. Typically, a series of $\sim$10 scans could be acquired before the effects of beam damage were observed even with this modified procedure. The profiles from the individual scans were then summed to yield a composite profile of spectra with $\sim$2 s total acquisition per pixel. Characteristic X-ray intensity profiles were extracted from the composite spectrum profiles, which allowed improved background fitting relative to comparable spectra from individual pixels, using the multiple linear least-squares (MLLSQ) fitting routine of Desk-Top Spectrum Analyzer (DTSA; Fiori et al. 1992).

LV-EDX spectrum imaging

Low-voltage EDX spectrum images were acquired with a Philips XL30 SEM equipped with a Schottky FEG, an
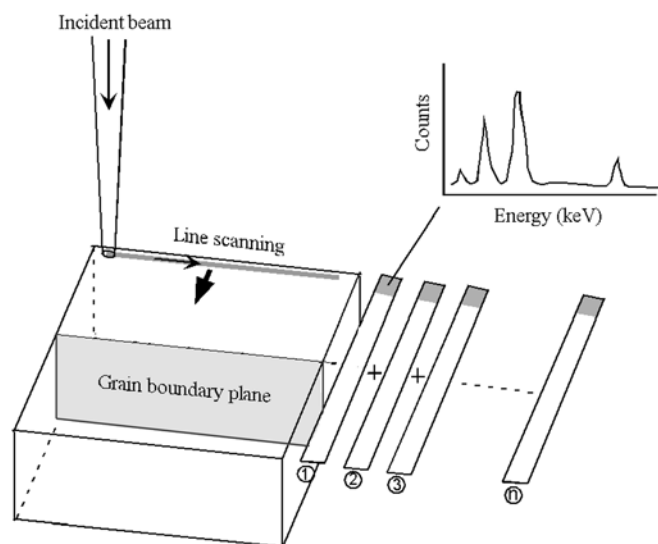

Fig. 1. Schematic representation of method of STEM/EDX profiling in this study. The grain boundary plane is nearly edge-on to the incident electron beam. Line scanning parallel to a grain boundary provides X-ray counts at a fixed distance from a grain boundary within the time increment corresponding to a single pixel without pausing the beam at any one location on the sample. Multiple equivalent line scans 1, 2, 3, ... *n* are collected; all lines scans following visible onset of damage are discarded. Spectra characteristic of a given position relative to the boundary are formed by summing equivalent spectra in sequential line scans

Oxford EDX detector with a super atmospheric thin window and XP3 pulse processor, and an ES Vision integrated acquisition system. The specimen was oriented normal to the incident electron beam and the take-off angle for acquisition was 35°. The microscope was operated at 4 kV, at which the demonstrated spatial resolution is $\sim$160 nm based on analysis of a silicon-based semiconductor chip (Anderson 1999). A 30 μm final aperture was used, and the condenser lens excitation was selected to yield an X-ray count rate of $\sim$1,500/s. Spectrum images of 200$\times$200 pixels were acquired with a pixel spacing of 100 nm, so that 20$\times$20 μm regions of the specimens were mapped. The dwell time per pixel was 1 s, for a total acquisition time of $\sim$11 h per spectrum image.

EDX spectrum imaging is complementary to elemental mapping with the electron microprobe (EPMA). The limited spectral resolution of EDX ($\sim$135 eV at Mn-K_α) relative to that achievable with the wavelength dispersive X-ray (WDX) spectrometers of the EPMA is balanced by the parallel spectral acquisition of EDX which allows a full spectrum, rather than a limited number of X-ray intensity maps to be acquired at each pixel. The principle benefit of X-ray microanalysis at low (typically 5 kV) operating voltages is the higher spatial resolution which can be achieved relative to the $\sim$25 kV operating voltage of an EPMA (Boyes 1994; Nockolds 1994). The drawback is that X-rays with inner-shell excitations of higher energy than the operating voltage are not excited, so that suitable X-ray lines may not be present to characterize all elements in the sample. For example, in the maps acquired for this study, the 4-keV incident electron energy precluded the characterization of the calcium distribution, since the inner-shell ionization energy for Ca-K (4.038 keV) is higher than the incident electron energy, and the effective yield of the Ca-L X-rays is too weak to be detected.

Results

LV-EDX spectrum imaging

Al-K and Fe-L maps of the olivine + 12 vol% basalt and the lherzolite samples in Fig. 2 reveal that Al is normally restricted to glass-filled, three- and four-grain junctions. Occasionally, glass is present in pockets along grain boundaries. Glass was not detected at grain boundaries at the resolution of the LV-EDX spectrum imaging. The presence of facetted grains around many glass pockets demonstrates the anisotropy of the melt-olivine interfacial energy. In the olivine + basalt sample, the Fe concentration is enhanced in the olivine grains both near phase boundaries with melt and near grain boundaries. In the lherzolite sample, Fe-enrichment is present at fewer crystal-melt phase boundaries, and the degree of enrichment is correspondingly smaller than in the olivine + basalt
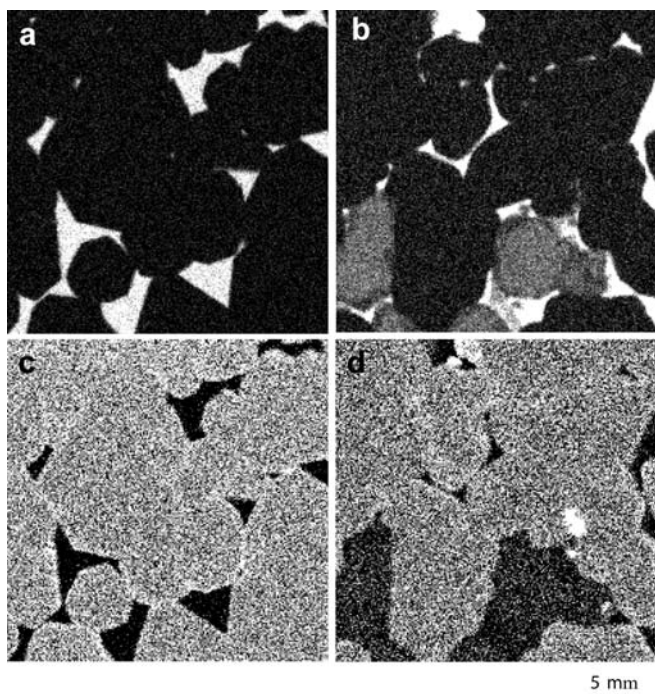
Fig. 2a–d. LV-EDX spectrum imaging maps of olivine + basalt and lherzolite samples. The Y-axis of the maps is parallel to the maximum principle stress, O_1. **a** Al-K, and **b** Fe-L maps of olivine + basalt. **c** Al-K, and **d** Fe-L maps of lherzolite. *Darkly* and *lightly shaded* grains in **c** are olivine and orthopyroxene, respectively

Fig. 3a, b. TEM and HREM images of a grain boundary in an olivine + 2 vol% basalt sample. **a** TEM image showing large-scale structure of the boundary. **b** HREM image and diffraction pattern of the area indicated by the *arrow* in **a**

specimen; no enrichment was observed at any of the grain boundaries. The width of the enriched region in the LV-EDX Fe-L maps is similar to the spatial resolution, $\sim$150 nm, which provides an upper limit on the spatial extent of the Fe-enriched near-boundary regions.

HREM

Grain boundaries with no glass phase

TEM and HREM images of a boundary between olivine grains in the olivine + 2 vol% basalt sample are shown in Fig. 3. The HREM image was acquired from the region of the grain boundary indicated by an arrow in the TEM image. In the HREM image, the two crystalline grains joined at the boundary exhibit (021) and (002) lattice fringes. No other phases were observed, even at less than a nanometer scale. Similar TEM and HREM images of a boundary between olivine grains in the lherzolite (9 vol% glass) sample are presented in Fig. 4. Although not shown in the TEM image, the boundary is connected to a glass pocket in a nearby triple junction. Based on the HREM image, we determined that the boundary plane is rotated $\sim$9° from (021) of the upper olivine grain. The boundary plane is not completely straight, but it is faceted with many steps along (021). The lattice fringes of both grains are directly connected,
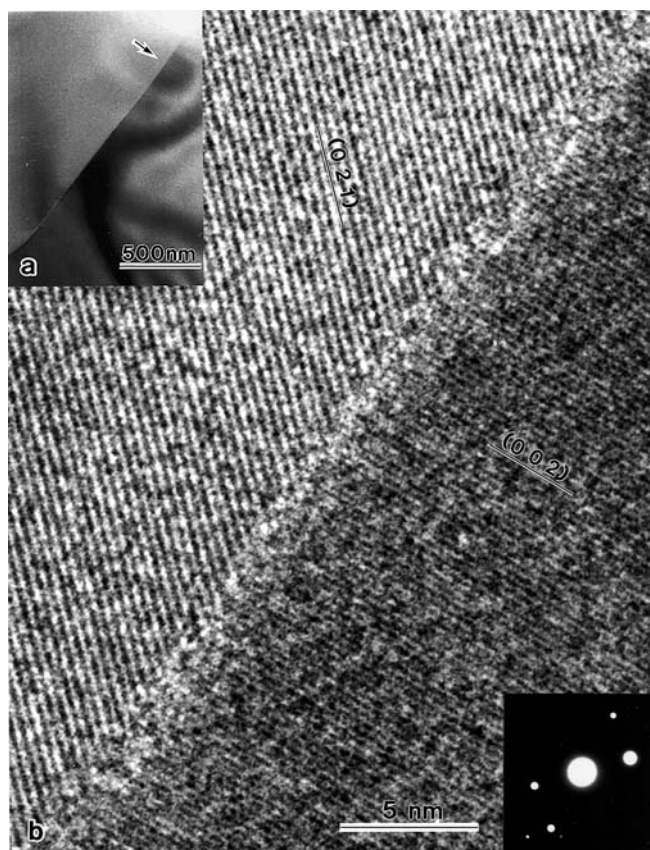
excluding the possibility of a distinct grain boundary phase.

Among the boundaries observed in both the olivine + basalt and lherzolite samples, some exhibit points of strain contrast along them, as illustrated in Fig. 5. Based on the diffraction patterns, the boundaries are not low-angle grain boundaries characterized by periodic arrays of dislocations accommodating a misfit of neighboring grains. In Fig. 5a, the TEM image shows that the boundary is connected to a glass pocket in a three-grain junction formed by olivine grains. The strain contrast appears to be non-periodic. Based on the HREM image, the boundary is parallel to (101) of the lower olivine grain, with no detectable boundary phase. In the boundary, arrows denote some steps, but the distribution of the steps is not related to the points of strain contrast.

As we mentioned above, HREM analysis of grain boundary structure is only possible for edge-on boundaries which satisfy specific diffraction conditions in the neighboring grains. Therefore, the number of boundaries with > 10° misorientation which could be analyzed was 15. None had specific crystallographic relationships such as a coincident site lattice (CSL) relationship, and none contained a thin glass film.
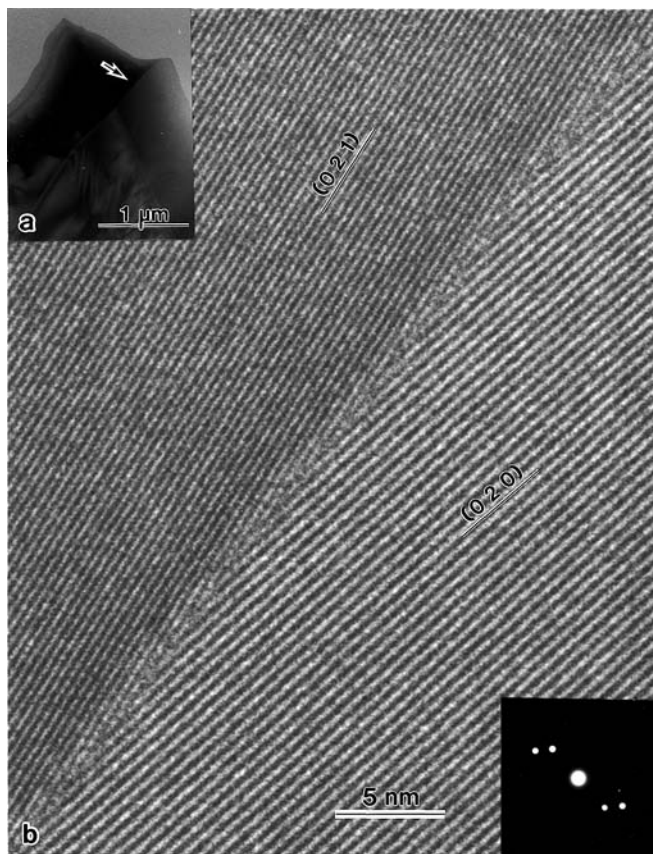
Fig. 4a, b. TEM and HREM images of grain boundary in the partially molten lherzolite sample with 9 vol% melt. **a** TEM image showing the large-scale structure of the boundary. **b** HREM image and diffraction pattern of the area indicated by the *arrow* in **a**

Grain boundaries with a glass phase

The glass phase in the grain boundary shown in Fig. 6 is clearly distinguishable from the olivine grains, which exhibit (111) and (021) lattice fringes. The glass region exhibits a lighter contrast than the olivine grains and has a "mazy contrast" which is characteristic of amorphous materials. The thickness of the glass is almost constant at ~11 nm in the region of this image. The image shows that the boundary between the glass and the grain is parallel to (121) of the grain on the right.

A series of images acquired from a single boundary at different magnifications is shown in Fig. 7. The boundary is connected to a glass-filled triple junction surrounded by olivine and pyroxene grains (Fig. 7a). The thickness of the glass phase extending along the boundary decreases with increasing distance from the triple junction (Fig. 7b–d), forming a taper. The HREM image reveals that the boundary between the glass and the grain is parallel to (101) of the olivine grain on the right.
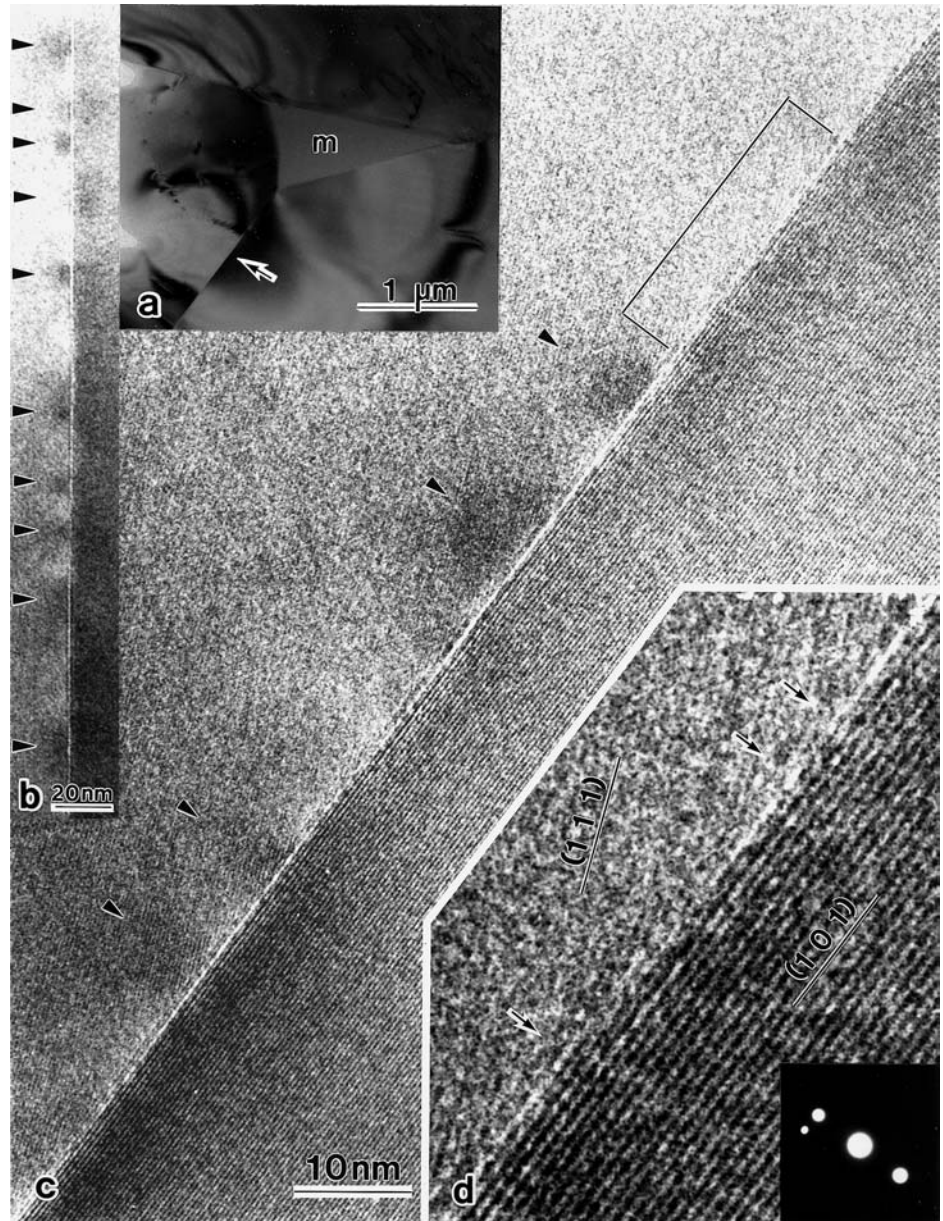
Dark band in grain boundaries

Occasionally, a dark band is observed to separate two grains. Two images acquired at the same place but with a relative defocus of 48 nm between the images are presented in Fig. 8. The thickness and contrast of the dark band decrease with increasing defocus, and the lattice fringes around the boundary become sharper accordingly. We could not detect the presence of a grain boundary phase in these two images.

STEM/EDX profiling

We analyzed more than five olivine grain boundaries in both olivine + 12 vol% basalt and lherzolite samples. All the boundaries are similar to the boundary shown in the TEM image of Fig. 9. In the image, the continuation of the straight boundary into the glass-filled triple junction indicates that the boundary plane corresponds to a low-index crystallographic plane of the lower olivine grain. Since this type of boundary is a planar feature in the depth direction, it is possible to bring the boundary to the edge-on orientation. As shown in the image, diffraction contrast remains after the analysis, demonstrating that sample damage is not serious enough to cause significant destruction of the crystalline lattice. The chemical profiles by STEM/EDX analysis in Fig. 10 are from the boundary shown in Fig. 9. In Fig. 10, X-ray counts are plotted versus distance from the boundary. For reference, X-rays from a glass pocket with about the same thickness are plotted in the right-hand column of Fig. 10a. Mg and Si are slightly depleted at the boundary, whereas other major elements such as Fe and O are constant across the boundary. The boundary composition is clearly different from that of the glass phase. The enrichments of Ca and Ti at the boundary are roughly in proportion to their relative concentrations in the glass. The statistical significance of the enhanced Al signal at the boundary is questionable, especially given the situation of the K X-ray peak of Al between those of Mg and Si, which have concentrations at least two orders of magnitude larger than that of the Al, even in the spectrum from the middle of the boundary. As a result, precise background correction was not possible for the Al signal. The small negative systematic error (~40 counts) in the Al signal away from the boundary is indicative of the difficulty in quantify the Al signal at this weak level. The experimentally measured width of the grain boundary segregation is ~7 nm. However, in the thickness regime necessary to acquire sufficient signal, this width may be indicative of beam broadening effects, and hence the ~7 nm measured width is an upper bound on the true chemical width of the boundary. Additional degradation of the spatial resolution may also have resulted because of instabilities in the position of the beam relative to the boundary when the beam returns to the left-hand side of the image to begin a new line scan (the "fly back") during data acquisition. In the conventional ES Vision spectrum imaging mode, no X-rays are collected during this resetting of the beam position. However, with our modified procedure, X-rays excited during the resetting of the beam contribute to the spectrum.

Fig. 5a–d. TEM and HREM images of a grain boundary parallel to low-index crystallographic plane in the olivine + 12 vol% basalt sample. **a** TEM image showing the large-scale structure of the boundary indicated by the *arrow*. *M* Melt (glass). **b** *Arrows* show nonperiodic strain contrast along the boundary. **c** HREM image showing that the boundary plane is parallel to the *(101)* plane of the grain on the *right*. Strain contrast is indicated by *arrows*. **d** Enlarged image of region free of strain contrast indicated in the *upper right* part of **c**. *Arrows* indicate steps in the boundary, showing that the steps do not correspond to the positions of strain contrast

Similar grain boundary segregation to that shown in Fig. 10 has been observed in other scans along this and other similar boundaries.

Corresponding profiles at a boundary from the lherzolite sample are shown in Fig. 11. Due to a diffraction effect, counts from major elements in the right-hand grain are slightly higher than those in the left-hand grain and do not indicate different compositions. Many aspects of the profile are quite similar to those from the olivine + basalt sample, except that significantly more Al is present in this boundary.

The sharpness of the profile peaks obtained near grain boundaries can be easily changed due to grain boundary tilting, grain boundary flatness, and alignment of the grain boundary with respect to the scanning direction of the electron beam. Although the profiles shown in Figs. 10 and 11 have the sharpest peaks obtained from both samples, the trends of these elements around grain boundaries are similar from one boundary to the next, indicating that the chemical features of the boundaries are common for all grain boundaries in the samples.

Discussion

Grain boundary structure

In many of the HREM images from each of the samples, the lattice fringes of neighboring grains meet along the grain boundaries with no detectable second phase. Thus, we conclude that most of the boundaries do not contain a thin glass film. This structure appears to be stable, such that melt will not infiltrate a melt-free grain
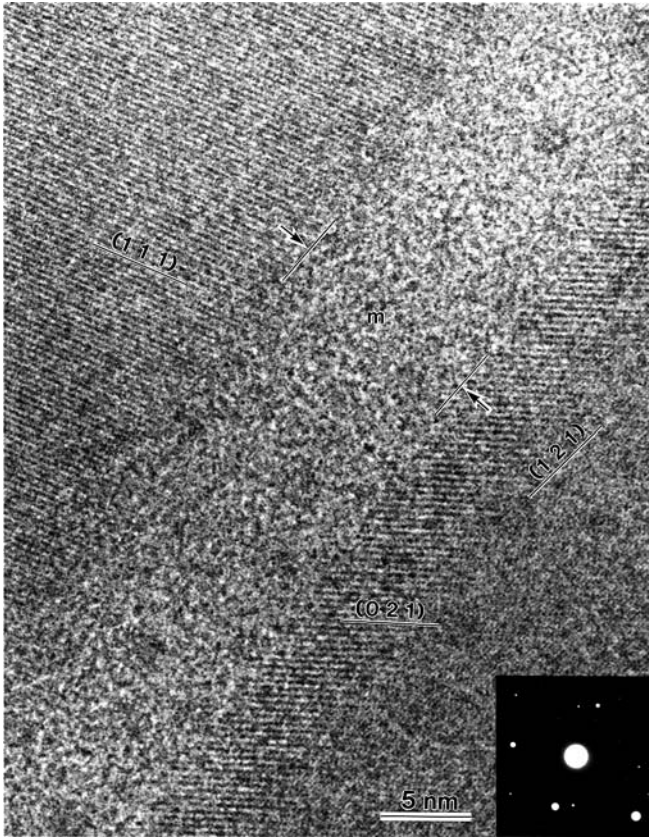
Fig. 6. HREM image and diffraction pattern of a boundary with a relatively thicker layer of glass in the olivine + 12 vol% basalt sample. Grains are distinguished by the presence of lattice fringes, whereas the glass exhibits typical amorphous contrast. The *right side* of the glass-grain interface is parallel to the *(121)* plane of the grain on the *right*

boundary. Likewise, if melt is present along boundary after hot-pressing, it will be expelled.

The points of strain contrast observed along some boundaries are indicative of dispersive structural distortions of neighboring grains. This distortion can be caused by dislocations or impurities. Since dislocations develop to maintain continuity of neighboring grains at boundaries, the grains must have a specific crystallographic relation such as a CSL relationship or a low-angle ($< 10°$) crystallographic difference. However, such structured relationships were not found using a Kikuchi diffraction pattern method to identify crystallographic orientations of the grains. In addition, no chemical differences existed between grain boundaries which did or did not exhibit this type of strain contrast.

Glass does exist along some boundaries, as observed in the HREM images in Figs. 6 and 7. However, we have not observed thin glass films with a uniform thickness on the order of a nanometer along any of the grain boundaries. Glass often tapers from a triple junction into a grain boundary, slowly decreasing in width with increasing distance from the triple junction, as shown in Fig. 7. In such cases, the wetting angle is very small ($\sim 2°$; Fig. 7b). Low-index crystallographic planes such

as (101) and (121) define boundaries which contain a glass phase. This observation agrees with a previous study of melt distribution at two-grain junctions at the SEM scale, in which flat faces with low-index crystallographic planes are dominantly wetted (Jung and Waff 1998). Thus, we conclude that the melt in the boundaries is stable if at least one olivine grain features a low-index boundary plane.

Chemistry of the grain boundaries

Fe-enrichment at some olivine-olivine boundaries and olivine-glass interfaces, as seen in the LV-EDX spectrum images in Fig. 2b, d, could be explained by Mg–Fe exchange between olivine and melt during the experiment and/or during the quenching process. The STEM-EDX measurements in Figs. 10 and 11, which sample within ~ 15 nm of the interface, demonstrates that the Fe-enrichment does not correspond to a spike in concentration at the boundary plane, but rather must extend throughout a near-boundary layer some tens of nanometers wide, such that no concentration gradient is apparent immediately adjacent to the boundary. The enrichment observed even in some glass-free grain boundaries in the olivine + basalt sample suggests that melt was initially present during the hot-press and then excluded during annealing and deformation. Because this sample was fabricated from a mixture of San Carlos olivine plus mid-ocean ridge basalt powders, it is likely that the olivine and basalt were not in chemical equilibrium prior to the experiment. By contrast, melt produced during the experiment on the lherzolite sample was initially formed at energetically favored areas such as triple-grain junctions but not at two-grain junctions. This difference may account for the Fe-enrichment in some grain boundaries in the olivine + basalt sample, but not in those in the lherzolite sample. Although the quenching time is short, grain overgrowth may still cause the Fe-enrichment in olivine grains at the contact with melt, as observed in both samples.

Prior to discussing the chemical features of the grain boundaries in Figs. 10 and 11, we must account for the effect of grain boundary grooving on the composition profiles. Even with low-angle ion milling, boundaries may still be thinner than the adjoining grains due to preferential thinning. Thickness affects the total X-ray counts. Since O is the only anion in the samples, its concentration must be approximately constant in order to maintain charge balance everywhere. In the profiles, depletion of O at the grain boundaries is within the range of detection error. Hence, any preferential thinning has had a negligible effect on the profile. Therefore, the profiles are characteristic of the true chemical variation in all of the scanned areas. To optimize the counting statistics, we selected an area with a greater thickness than the area imaged by HREM. The ~ 7 nm measured width of the EDX profiles thus represents the maximum width of the actual distribution of segregants,

Fig. 7a–d. TEM and HREM images of a region of a grain boundary containing a glass phase. **a** Grain boundary indicated by *arrow* is connected to the glass pocket in a triple junction formed by olivine and pyroxene grains. **b** Enlarged image of **a**. It is clear that the glass phase penetrates to the boundary. *Arrows* indicate the position of images in **c** and **d**. **c** HREM image from the region marked by upper *arrow* in **b**. Crystalline and glass phases are distinguished by lattice fringes and typical amorphous contrast, respectively. *Arrows* define the boundaries of the glass phase. The *right side* of a glass-grain interface is parallel to the *(101)* plane of the grain on the *right*. **d** HREM image from the region marked by the lower *arrow* in **b**. It is clear that the width of the glass phase narrows with increasing distance from the pocket
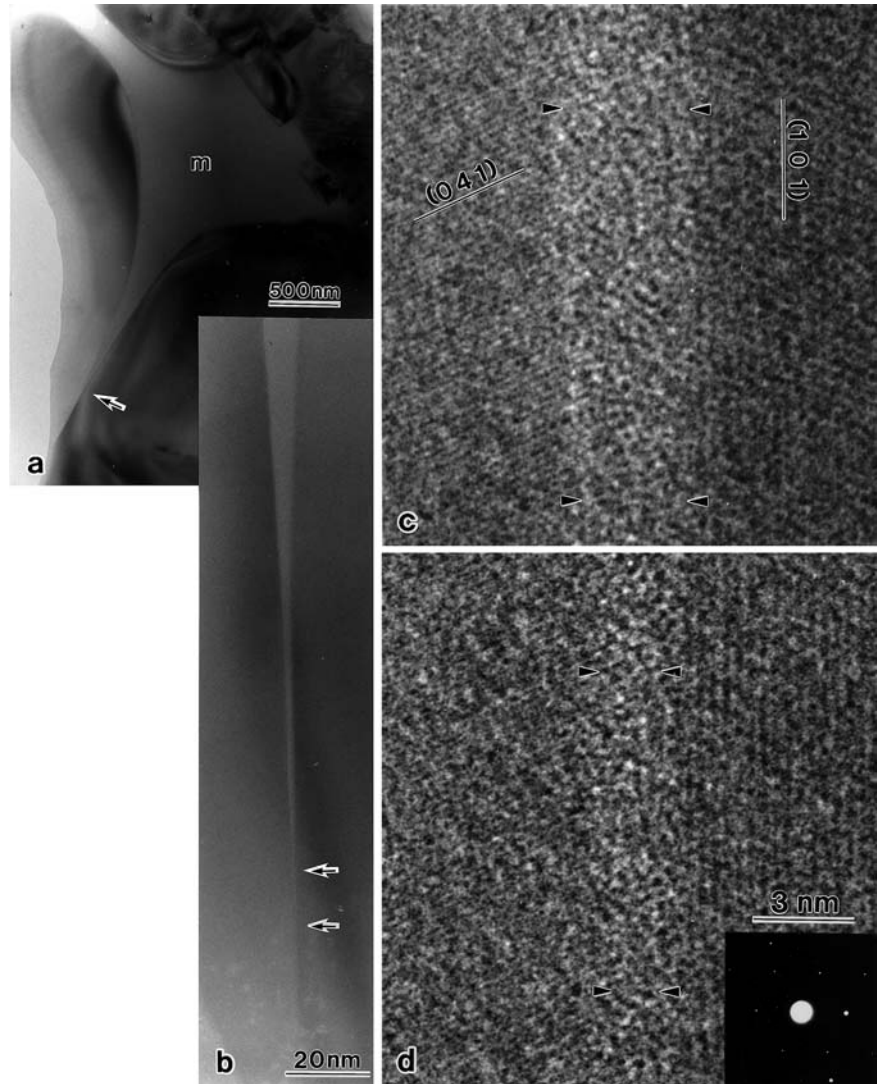
which is likely much smaller. The measured grain boundary concentration of the elements with low solubility in olivine provide only a lower bound for the actual concentrations, since even at the grain boundary plane the beam spreads into the adjacent intragranular regions, although these measurements are proportional to the actual grain boundary concentrations.

Ca, Al and Ti, which are primary components of the glass phase but only trace elements in olivine, are enriched in a region within ~ 7 nm of the grain boundaries (Figs. 10, 11). However, even if the chemical probing of the boundaries includes intragranular material or material formed by crystal growth during quenching which may change the grain boundary composition, the following chemical evidence demonstrates that the composition of the boundary is different from the composition of the bulk glass phase: (1) weak Si depletion occurs at the boundaries; and (2) Al segregation is much weaker than Ca segregation in the olivine + basalt sample. The glass phase has slightly lower contents of MgO and FeO but higher contents of SiO_2 compared

to typical basalt composition, as shown in Table 1. This chemical signature may be due to grain overgrowth during quenching. Even though the glass composition may have been changed from that at high temperature and pressure, the fact that the glass contains less MgO and more SiO_2 than olivine is consistent with many studies of the olivine-basalt system. Therefore, Si enrichment should be observed at the boundaries in both samples, if a glass phase exists at the boundaries or has been eliminated by crystal growth during quenching. In the olivine + basalt sample, the concentrations of Ca and Al in the glass phase are almost identical (Fig. 10a and Table 1). Therefore, the enrichment of Ca and Al at the boundaries should be similar, if a glass phase is present. Although the composition of the glass phase is very similar in the olivine + basalt and the lherzolite samples, significantly less Al has segregated to grain boundaries in the former. Possibly this difference is related to the fact that the olivine + basalt sample was deformed under hydrous condition whereas the lherzolite sample was deformed under anhydrous conditions.
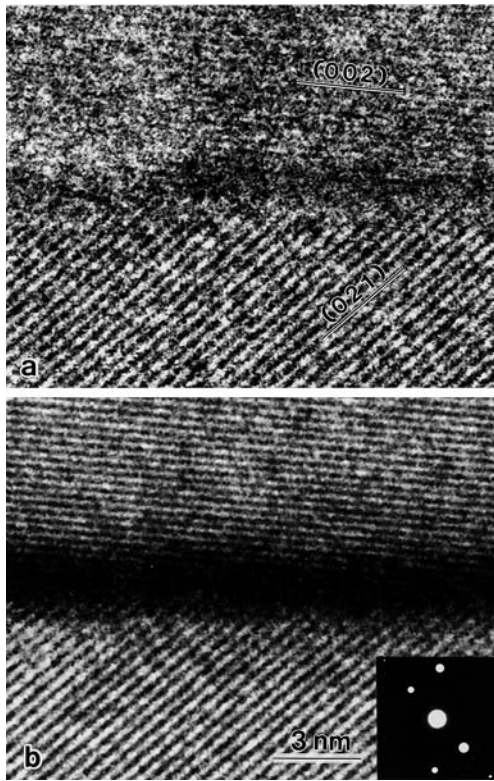
Fig. 8a, b. HREM images taken from a single place on the boundary but at different focus conditions. **a** Image taken –48 nm under focus from the condition of the image in **b**. **b** Lattice fringes of both grains are clearer than in **a** but a dark *band* appears along the boundary
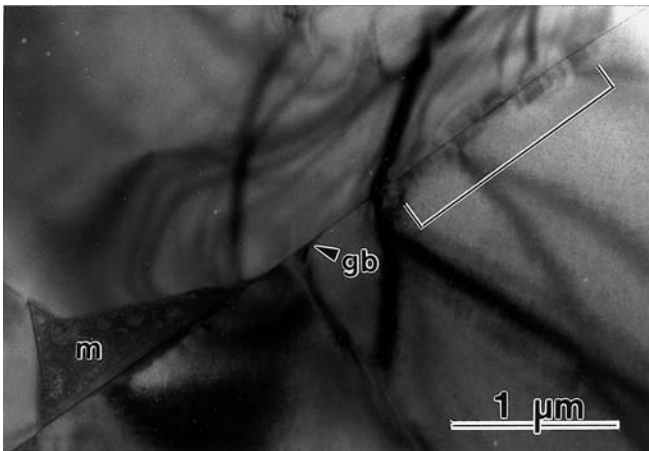

Fig. 9. TEM image of an area analyzed by STEM/EDX in the olivine + 12 vol% basalt sample. The *upper right* part of the boundary was decorated by contamination during the analysis (*gb* grain boundary)

Taking into account the HREM results, we conclude that the observed chemical profiles are due to segregation of Ca, Al and Ti to solid-solid interfaces. Correlation between the results of Wanamaker and Kohlstedt (1991) and our results may give a clue to understanding these chemical anomalies. From measurements of the wetting
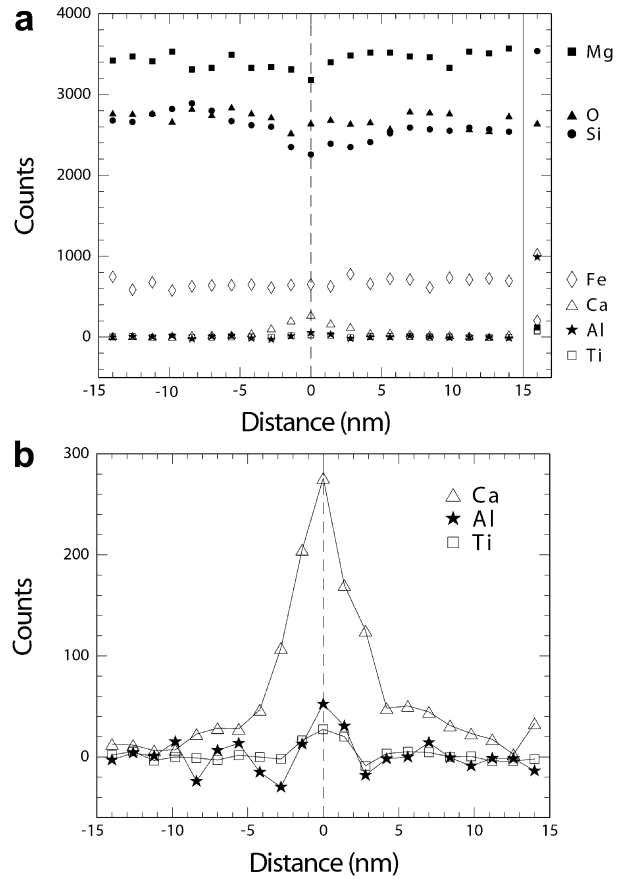

Fig. 10a, b. X-ray intensity profiles from STEM/EDX analysis for elements in the vicinity of the grain boundary in the olivine + basalt sample shown in Fig. 9. **a** Profiles are shown for seven elements. X-ray intensities from the glass phase in a triple junction are combined as a reference in the *right-hand column*. **b** Profiles in **a** for Ca, Al and Ti with an expanded intensity scale. The relative segregation of Ca and Ti is proportional to that in the glass, whereas the segregation of Al is relatively small

angles between olivine and melts of various compositions, these authors determined that the difference in wetting angles was due to CaO and Al_2O_3 excess or SiO_2 depletion at the olivine-melt phase boundary. Although the types of interfaces examined in the two cases are different, i.e., solid-solid in our study versus solid-melt in theirs, the similarities are very interesting. The segregation at the grain boundaries may be remnants of the melt-solid interfaces. However, this hypothesis may not apply to boundaries in the lherzolite samples, because boundary formation due to grain contacts was considered not to be dominant in the lherzolite, as discussed above. In addition, similar segregation is observed in melt-free olivine + diopside aggregates (Hiraga et al., unpublished data), indicating that the segregation can occur without the presence of a melt phase.

Comparisons with previous studies

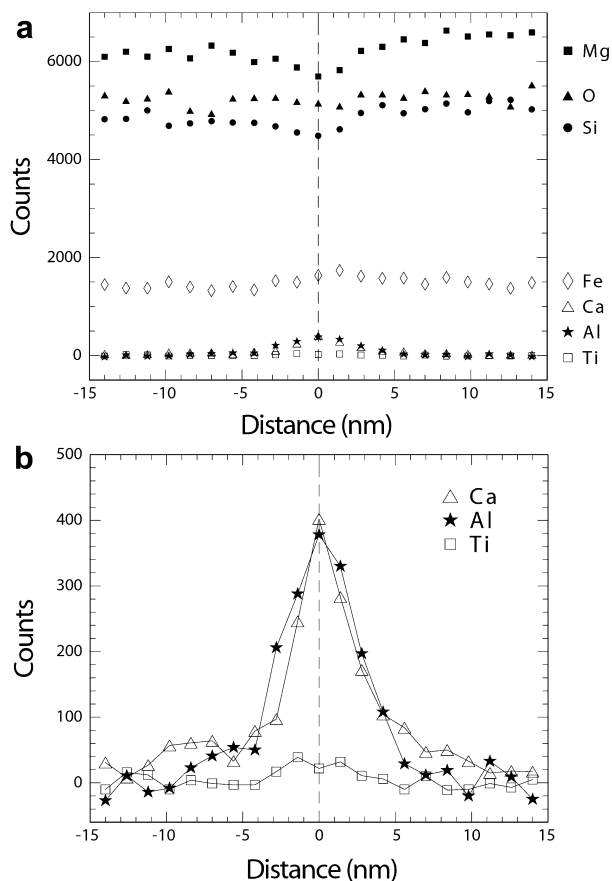Our conclusion that grain boundaries are melt-free but contain segregated elements differs from the conclusion

Fig. 11a, b. X-ray intensity profiles from STEM/EDX analyses for elements in the vicinity of the grain boundary in the lherzolite sample. **a** Profiles are presented for seven elements. **b** Profiles in **a** for Ca, Al and Ti with an expanded intensity scale. Segregation of Al is much greater than that observed in the olivine + basalt specimen in Fig. 10. Relative segregation of Ca and Al are comparable to those in the glass, whereas the segregation of Ti is relatively large

the darker band in Fig. 8b. Since the width and the contrast change significantly with change in the focus condition, we argue that this band is a Fresnel fringe. Fresnel fringes appear due to the different phase shifts experienced by the electron beam as it passes through materials of different mean inner potential. Therefore, fringes appear if a thin film exists. However, fringes may also appear even if a grain boundary is structured (i.e., free from a grain boundary phase), such as in the case of a dislocation-accommodated boundary or a twin boundary (Stobbs and Smith 1981; Rühle and Sass 1984; Simpson et al. 1986). Their presence has been attributed to the occurrence of a local, mean inner potential difference due to the lower density of the core of the dislocations, the segregation of impurities to these cores, or grooving of the grain boundary. Therefore, we argue that their HREM images are inconclusive and that these images could also be from film-free boundaries.

De Kloe et al. (2000) also used the Fresnel fringe method to determine the thickness of the film. However, measurement of the film thickness by this imaging technique gives a width 20 to 35% wider than the actual thickness, due to uncertainty in the exact location of fringe maximum (Clark 1979; Cinibulk et al. 1993). This error explains the width of the black band in De Kloe et al. (2000), which may be the Fresnel fringe itself (see above). Vaughan et al. (1982) obtained the same Fresnel fringe and DDF results as those of De Kloe et al. (2000). However, Vaughan et al. (1982) attributed their results to preferential thinning and associated thicker carbon coating at the boundaries. They concluded that the boundaries are film-free to a resolution of 2 nm, based on their HREM results.

As discussed above, melt can exist at a boundary when a low-index plane of olivine forms one side of the melt-solid interface. This situation explains the results of a DDF image in De Kloe et al. (2000, their Fig. 6), which shows amorphous material running continuously into the boundary with the same flat surface of the neighboring glass pocket and the boundary.

The absence of melt films in the boundaries examined in this study cannot be attributable to insufficient time at temperature to achieve structural equilibrium. De Kloe et al. (2000) argued that 177 min at 1,227 °C is insufficient, since they did not observe a film in some boundaries, but that 575 min at 1,200 °C is sufficient to form the film in all the boundaries. Our experimental times fall between these values. Some samples we examined have melt fractions which are more than 10 times that in the samples of De Kloe et al. (2000) and Drury and Fitz Gerald (1996). De Kloe et al. (2000) reported a grain size of 2 to 7 and 0.5 to 16 μm for their samples. These values are not substantially different from the grain size of our samples (5–10 μm in olivine + basalt samples, 4–8 μm in the lherzolite sample). Thus, assuming that melt infiltrates into the boundaries to obtain structural equilibrium, our samples should require much shorter time to attain that state, due to the much larger melt fraction present in melt pockets. However, we do not see any

reached by some other researchers (Drury and Fitz Gerald 1996; De Kloe et al. 2000). Their evidence for the presence of melt films can be summarized as follows: (1) observations of intergranular thin films with a thickness of 0.6 to 3.0 nm by HREM and Fresnel fringe imaging; (2) confirmation of the amorphous structure of these films by DDF imaging; and (3) detection of enrichments of elements such as Si, Ca and Al and depletion of Mg at grain boundaries by EDX analysis and energy filtering imaging. Many of these observations are consistent with ours. However, our interpretation of these results differs from theirs, as discussed below.

In their HREM images, De Kloe et al. (2000, their Figs. 11b and 12) argued that black bands ~1 nm thick correspond to a glass phase (i.e., quenched melt). However, as shown in Figs. 6 and 7, the glass phase should have amorphous contrast in their HREM image. Examination of their HREM images reveals lattice fringes extending into the band. Thus, we conclude that the band does not necessarily represent a grain boundary phase. The contrast and the width of the band are comparable to those of

Table 1. Chemical composition of grain boundaries and glass phases in the samples of olivine + 12 vol% basalt and lherzolite with 9 vol% melt

Analyzed area	MgO (wt%)	FeO	SiO$_2$	CaO	Al$_2$O$_3$	TiO$_2$	Cr$_2$O$_3$	Na$_2$O	MnO	K$_2$O
Grain boundary in olivine + basalt	49.1	8.0	37.8	3.3	0.9	0.4	–	–	–	–
Grain boundary in lherzolite	45.0	10.4	38.4	2.5	3.1	0.2	–	–	–	–
Glass pocket in olivine + basalt[a]	2.0	3.3	56.3	11.5	20.7	1.8	0.1	2.8	0.2	0.2
Glass pocket in lherzolite[a]	4.0	6.0	56.0	13.0	20.7	0.3	0.1	1.9	–	0.1

[a]Analysis by EPMA

evidence for the presence of melt films, even as a transient feature in the boundaries near melt pockets.

As chemical evidence for the presence of melt films, Drury and Fitz Gerald (1996) and De Kloe et al. (2000) reported enrichment in Ca and Al at grain boundaries. In addition, De Kloe et al. (2000) also found depletion in Mg at boundaries. All of their qualitative results are consistent with our observations. Both papers mentioned Si enrichment at the boundaries. However, we could not find any evidence supporting this statement. In Fig. 15 of De Kloe et al. (2000), the X-ray intensity of Si in grain boundaries is slightly smaller than or comparable to that in the olivine grains.

These authors reported that the chemical anomalies for Mg and Si are not observed in an undeformed sample from the same material used in their deformation experiments. From this fact, they argue that melt films were not present at the beginning of the experiment and infiltrate into grain boundaries, acquiring a structural equilibrium state. However, based on our results, we suggest a different interpretation of their observations. We suggest that chemical segregation and depletion, which involve diffusion, were not completed in their starting material due to the short experimental time. Kohlstedt (1990) did not find chemical difference between intra- and intergranular areas, concluding the absence of melt films. In this case, rapid element loss during irradiation or difficulties in the exact positioning of the electron beam are possible reasons, as pointed out by De Kloe et al. (2000).

Therefore, we conclude that the results of Drury and Fitz Gerald (1996) and De Kloe et al. (2000) are consistent with our observations, which demonstrate that melt films are absent in partially molten ultra-mafic rocks but that segregation does occur to the grain boundaries. Melt is not stable as a thin film, but is stable as a somewhat thicker layer between olivine grains due to the effect of crystal anisotropy.

Geological implications

The conclusion that the grain boundaries in partially molten mafic rocks do not contain a thin melt film, even in samples with different amounts of melt (2 to 12 vol%) and with different mineral assemblages (olivine + basalt versus partially molten lherzolite), is consistent with the deformation properties of these rocks. It has been shown that if the melt fraction exceeds ~4 vol%, weakening due to the presence of melt significantly deviates from the predictions of the isotropic melt distribution model of Cooper and Kohlstedt (1986) (Hirth and Kohlstedt 1995; Mei et al. 2002; Zimmerman and Kohlstedt, unpublished data). From a microstructural point of view, this deviation may be due to the effect of anisotropic wetting properties. As melt fraction increases, olivine grains become more euhedral, with low-index crystal faces in contact with the melt. As discussed above, melt layers are stable along grain boundaries formed with low-index crystallographic planes, because of the anisotropy in the solid-melt interfacial energy which reaches its minimum value for low-index surfaces. The intergranular melt is a fast diffusion path and may also facilitate grain boundary sliding. Therefore, significant weakening occurs as melt fraction increases in the rocks. These processes are discussed in detail in Mei et al. (2002).

Chemical segregation observed in our experiments may play an important role in the rheology and chemistry of the rock. Segregation will influence grain boundary diffusivity of all chemical species. In addition, a boundary will act as a storage site for trace elements in the rocks, such that incompatible elements will be enriched at grain boundaries and the bulk concentration of these elements will depend on grain size (i.e., the ratio of boundary area to grain volume).

References

Anderson IM (1999) Quantitative chemical mapping with low-voltage EDX spectrum imaging and multivariate statistical analysis. Microsc Microanal 5 Suppl 2:318–319

Boyes E (1994) High resolution imaging and microanalysis in the SEM at low voltage. In: Proc 13th Int Congr Electron Microscopy 1, pp 51–54

Cinibulk MK, Kleebe H-J, Rühle M (1993) Quantitative comparison of TEM techniques for determining amorphous intergranular film thickness. J Am Ceram Soc 76:426–432

Clarke DR (1979) On the detection of thin intergranular films by electron microscopy. Ultramicroscopy 4:33–44

Clarke DR (1987) On the equilibrium thickness of intergranular glassy phases in ceramic materials. J Am Ceram Soc 70:15–22

Cooper RF, Kohlstedt DL (1986) Rheology and structure of olivine-basalt partial melts. J Geophys Res 91:9315–9323

Daines MJ, Kohlstedt DL (1993) A laboratory study of melt migration. Philos Trans R Soc Lond A 342:43–52

De Kloe R, Drury MR, van Roermund HLM (2000) Evidence for stable grain boundary melt-films in experimentally deformed olivine-orthopyroxene rocks. Phys Chem Miner 27:480–494

Drury MR, Fitz Gerald DF (1996) Grain boundary melt-films in upper mantle rocks. Geophys Res Lett 23:701–704

Fiori CE, Swyt CR, Myklebust RL (1992) Desktop spectrum analyzer and X-ray database (DTSA). http://www.cstl.nist.gov/div837/Division/outputs/DTSA/DTSA.htm

Hirth G, Kohlstedt DL (1995) Experimental constraints on the dynamics of the partially molten upper mantle: Deformation in the diffusion creep regime. J Geophys Res 100:1981–2001

Hwang CJ, Chen IW (1990) Effect of a liquid phase on superplasticity of 2-mol%-Y_2O_3-stabilized tetragonal zirconia polycrystals. J Am Ceram Soc 73:1626–1632

Jung H, Waff HS (1998) Olivine crystallographic control and anisotropic melt distribution in ultramafic partial melts. Geophys Res Lett 25:2901–2904

Kingery WD (1974) Plausible concepts necessary and sufficient for interpretation of ceramic grain-boundary phenomena: II, solute segregation, grain-boundary diffusion, and general discussion. J Am Ceram Soc 57:74–83

Kohlstedt DL (1990) Chemical analysis of grain boundaries in an olivine-basalt aggregate using high-resolution, analytical electron microscopy. Geophys Monogr 56:211–218

Mei S, Bai W, Hiraga T, Kohlstedt DL (2002) Influence of melt on the creep behavior of olivine-basalt aggregates under hydrous conditions. Earth Planet Sci Lett 201:491–507

Nockolds CE (1994) Low-voltage electron probe X-ray microanalysis in an in-lens field emission gun SEM: an evaluation. Microbeam Anal 3:185–189

Paterson M (1990) Rock deformation experimentation. Geophys Monogr Am Geophys Union 56:187–194

Rasmussen DR, Simpson YK, Kilaas R, Carter CB (1989) Contrast effects at grooved interfaces. Ultramicroscopy 30:52–57

Rühle M, Sass SL (1984) The detection of the change in mean inner potential at dislocations in grain boundaries in NiO. Philos Mag A 49(6):759–782

Simpson YK, Carter CB, Morrissey KJ, Angelini P, Bentley J (1986) The identification of thin amorphous films at grain-boundaries in Al_2O_3. J Mater Sci 21:2689–2696

Stobbs WM, Smith DJ (1981) A high resolution study of twin boundary structure in copper. In: Electron microscopy and analysis. Institute of Physics, London, Conf Ser 61, pp 373–376

Vaughan PJ, Kohlstedt DL, Waff HS (1982) Distribution of the glass phase in hot-pressed, olivine-basalt aggregates: an electron microscopy study. Contrib Mineral Petrol 81:253–261

Wanamaker BJ, Kohlstedt DL (1991) The effect of melt composition on the wetting angle between silicate melts and olivine. Phys Chem Miner 18:26–36